

## Two-Component $\gamma$ -ray Emission Spectrum and X-Ray Polarization of the Radio Galaxy Pictor A

JIA-XUAN LI,<sup>1</sup> XIN-KE HU,<sup>1</sup> JI-SHUN LIAN,<sup>1</sup> YU-WEI YU,<sup>1</sup> WEI DENG,<sup>2</sup> KUAN LIU,<sup>2</sup> HAI-MING ZHANG<sup>†</sup>,<sup>3</sup> LIANG CHEN,<sup>4</sup>  
AND JIN ZHANG<sup>†</sup><sup>1</sup>

<sup>1</sup>*School of Physics, Beijing Institute of Technology, Beijing 100081, People's Republic of China; j.zhang@bit.edu.cn*

<sup>2</sup>*Guangxi Key Laboratory for Relativistic Astrophysics, School of Physical Science and Technology, Guangxi University, Nanning 530004, People's Republic of China*

<sup>3</sup>*School of Astronomy and Space Science, Nanjing University, Nanjing 210023, People's Republic of China; hmzhang@nju.edu.cn*

<sup>4</sup>*Key Laboratory for Research in Galaxies and Cosmology, Shanghai Astronomical Observatory, Chinese Academy of Sciences, 80 Nandan Road, Shanghai 200030, People's Republic of China*

### ABSTRACT

Pictor A is a  $\gamma$ -ray emitting radio galaxy and has a bright hotspot called WHS, located  $\sim 4$  arcmin away from the nucleus. In this letter, we present an analysis of its 16-year Fermi-LAT data and report the first Imaging X-ray Polarimetry Explorer (IXPE) observation for this source. Our analysis of the Fermi-LAT observations reveals evidence of two components in the average  $\gamma$ -ray spectrum of Pictor A, exhibiting a statistically significant hardening from  $\Gamma_{\gamma}^1 = 3.25 \pm 0.15$  to  $\Gamma_{\gamma}^2 = 1.81 \pm 0.07$  at a break energy of  $2.46 \pm 0.09$  GeV. The evident variability of  $\gamma$ -rays is observed in Pictor A. Interestingly, the variability is dominated by the component below the break energy, and the component above the break energy shows no variability. Furthermore, we find that a power-law function can adequately fit the spectrum during high-flux states, whereas a broken power-law is still required to explain the spectrum during low-flux state. We suggest that the low-energy component originates from the nucleus, while the high-energy component primarily stems from WHS. The broadband spectral energy distributions of both nucleus and WHS can be well represented by a simple leptonic model, with both  $\gamma$ -ray components attributed to the synchrotron-self-Compton (SSC) process. The analysis of IXPE data on the nucleus yields an upper limit to the polarization degree  $\Pi_X < 8.9\%$  in the 2–8 keV band, agreeing with its X-ray emission originating from SSC. However,  $\Pi_X = 23.5\% \pm 5.6\%$  is observed at a confidence level of  $> 99\%$  in the 5–7 keV band, and the possible physical origin of this narrow-energy-band polarization signal is discussed.

*Keywords:* galaxies: active—galaxies: jets—radio continuum: galaxies—gamma rays: galaxies—X-ray: polarimetry

### 1. INTRODUCTION

Radio galaxies (RGs), a subset of radio-loud Active Galactic Nuclei (AGNs), are distinguished by the presence of jet substructures that extend from the radio core to scales of kiloparsecs to megaparsecs (kpc–Mpc). Hotspots, characterized by high surface brightness at the edges of extended radio lobes in RGs, are considered to represent the jet termination, where magnetic fields are amplified and particles are accelerated to high energies (Meisenheimer et al. 1989; Thimmappa et al.

2022). Thanks to Chandra observations, numerous hotspots within RG jets have been detected in the X-ray band (Harris & Krawczynski 2006 for a review), however, ongoing debate persists regarding their X-ray radiation mechanisms (e.g., Kataoka & Stawarz 2005; Zhang et al. 2010, 2018). In addition, both the inverse Compton scattering and second synchrotron radiation models of X-rays predict the observable  $\gamma$ -ray emission for some large-scale jet substructures (Zhang et al. 2010, 2018; Wang et al. 2020; He et al. 2023).

The detection of  $\gamma$ -rays from large-scale radio lobes of RGs Cen A (Abdo et al. 2010; Sun et al. 2016; H. E. S. S. Collaboration et al. 2020), Fornax A (Ackermann et al. 2016), and NGC 6251 (Yu et al. 2024) confirms that the large-scale jet substructures

are acceleration sites of high-energy particles. To date, the Fermi Large Area Telescope (Fermi-LAT) has detected numerous RGs (Abdollahi et al. 2022; Ballet et al. 2023); however, the limited spatial resolution of Fermi-LAT makes it difficult to judge the location of the  $\gamma$ -ray emission for the majority of RGs. It has been proposed that some large-scale jet substructures may have the detectable  $\gamma$ -ray emission through the search for a steady  $\gamma$ -ray emission component and modeling of the broadband spectral energy distributions (SEDs; Guo et al. 2018; Zhang et al. 2018).

Pictor A is a  $\gamma$ -ray emitting RG, located at a redshift of  $z = 0.035$  (Schmidt 1965). It has a bright primary hotspot, known as the western hotspot (WHS), which is situated about 4 arcmin ( $\sim 165$  kpc) away from the radio core (Perley et al. 1997). Its nucleus is a strong X-ray source and has been widely studied; a PL spectrum is observed (Eracleous & Halpern 1998; Sambruna et al. 1999), maybe with a weak Fe K $\alpha$  line (Hardcastle et al. 2016). Extensive research has also been conducted on this bright WHS (Roeser & Meisenheimer 1987; Thomson et al. 1995; Perley et al. 1997; Tingay et al. 2008; Simkin et al. 1999; Wilson et al. 2001; Isobe et al. 2017; Sunada et al. 2022; Thimmappa et al. 2022; Gulati et al. 2023; Shaik et al. 2024). The observed flat spectrum and flux variability in the X-ray band suggest that the X-rays from WHS are produced by synchrotron radiation (Thimmappa et al. 2020; Sunada et al. 2022; Gulati et al. 2023; Shaik et al. 2024). X-ray polarization observations can serve as a valuable tool to verify its radiation mechanisms.

The  $\gamma$ -rays detected by Fermi-LAT for Pictor A are generally attributed to the contribution of the nucleus; adding the X-ray emission from the nucleus, they are produced through the synchrotron-self-Compton (SSC) process (Brown & Adams 2012; Xue et al. 2017; Gulati et al. 2023). However, it is also possible that the  $\gamma$ -rays stem from the WHS (Zhang et al. 2009). In this paper, we perform a comprehensive analysis of the  $\sim 16$ -year Fermi-LAT observation data to investigate the origins of  $\gamma$ -ray emission from Pictor A, and we examine the X-ray emission mechanisms of the nucleus and WHS using the first Imaging X-ray Polarimetry Explorer (IXPE; Weisskopf 2022) observation for Pictor A in conjunction with the broadband SED modeling. Observations and data analysis are given in Section 2, followed by the presentation of results in Section 3. The SEDs of the nucleus and WHS are constructed and modeled in Section 4. A discussion and conclusions are presented in Section 5.  $H_0 = 71$  km s $^{-1}$  Mpc $^{-1}$ ,  $\Omega_m = 0.27$ , and  $\Omega_\Lambda = 0.73$  are adopted in this paper.

## 2. OBSERVATIONS AND DATA ANALYSIS

### 2.1. *Fermi-LAT*

Pictor A is associated with  $\gamma$ -ray source 4FGL J0519.6-4544 in the 4FGL-DR4 (Abdollahi et al. 2022; Ballet et al. 2023). We select the data within  $15^\circ$  region of interest (ROI) centered on the radio position of Pictor A (R.A.= $79^\circ.957$ , Decl.= $-45^\circ.779$ ) and download the PASS 8 data covering from 2008 August 4 to 2024 July 10 (MJD 54682–60501) within the energy range of 0.1–500 GeV from the Fermi Science Support Center<sup>1</sup>.

The publicly available software `fermitools` (v.2.2.0) and `Fermipy` (v.1.1)(Wood et al. 2017) are used in our analysis. We use event class “SOURCE” (evclass=128) and event type “FRONT+BACK” (evtype=3) for the binned likelihood analysis based on LAT data selection recommendations<sup>2</sup> and set the maximum zenith angle of  $90^\circ$  in order to eliminate the contamination of  $\gamma$ -ray emission from the earth limb. A standard filter expression “(DATA\_QUAL>0)&&(LAT\_CONFIG==1)” and the instrument response function of P8R3\_SOURCE\_V3 are used in our analysis. All of the  $\gamma$ -ray source models included in the 4FGL-DR4 (Abdollahi et al. 2020) within the ROI and two background model including the isotropic emission (“iso\_P8R3\_SOURCE\_V3\_V1.txt”) and the diffuse galactic interstellar emission (“gll\_iem\_v07.fits”) are added to the model. Only the parameters of the sources within  $6.5^\circ$  centered on Pictor A and the normalization of two background model are left free.

We use the test statistic (TS) to evaluate the significance of a  $\gamma$ -ray source signal,  $TS = 2(\log \mathcal{L}_{\text{src}} - \log \mathcal{L}_{\text{null}})$ , where  $\mathcal{L}_{\text{src}}$  and  $\mathcal{L}_{\text{null}}$  are the likelihood values of the background with and without the target source, respectively. The TS map of the Pictor A region is shown in the left panel of Figure 1, the cyan cross show the best-fit position of the  $\gamma$ -ray source in this work, i.e., R.A. =  $79.91^\circ \pm 0.02^\circ$  and Decl. =  $-45.77^\circ \pm 0.02^\circ$ . This best-fit position is consistent with that of 4FGL J0519.6–4544 and spatially associated with Pictor A.

Note that there is a bright flat-spectrum radio quasar named PKS J0515–4556 (4FGL J0515.6–4556) located  $0.75^\circ$  away from Pictor A. As shown in the right panel of Figure 1, the maximum TS value of the residual TS map is  $\sim 4$ , indicating that the  $\gamma$ -ray emission from this source is well fitted by the model and no new  $\gamma$ -ray sources are found.

Pictor A is identified as a point-like source with a power-law (PL) spectrum in 4FGL-DR4

<sup>1</sup> <https://fermi.gsfc.nasa.gov/cgi-bin/ssc/LAT/LATDataQuery.cgi>

<sup>2</sup> <https://fermi.gsfc.nasa.gov/ssc/data/analysis/documentation/Cicerone/Ci>

(Abdollahi et al. 2022; Ballet et al. 2023). However, as shown in Figure 2(a), we observe that the spectrum of Pictor A is better described by a broken power-law (BPL) function than a PL function with a value of  $\Delta\text{TS} = 38.88$  (corresponding to a significance level of  $5.8\sigma$ ).  $\Delta\text{TS}$  is identified as  $\Delta\text{TS} = 2(\log\mathcal{L}_{\text{BPL}} - \log\mathcal{L}_{\text{PL}})$ , where  $\mathcal{L}_{\text{BPL}}$  and  $\mathcal{L}_{\text{PL}}$  are the likelihood values of BPL and PL functions, respectively. The PL function is defined as

$$\frac{dN(E)}{dE} = N_0 \times \left(\frac{E}{E_0}\right)^{-\Gamma_\gamma}, \quad (1)$$

and the BPL function is defined as

$$\frac{dN(E)}{dE} = N_0 \times \begin{cases} \left(\frac{E}{E_b}\right)^{-\Gamma_\gamma^1} & E < E_b \\ \left(\frac{E}{E_b}\right)^{-\Gamma_\gamma^2} & E \geq E_b \end{cases}, \quad (2)$$

where  $E_b$  represents the break energy,  $\Gamma_\gamma^1$  and  $\Gamma_\gamma^2$  are the index below and above the break energy, respectively. By analyzing the  $\sim 16$ -year Fermi-LAT observation data for Pictor A, we obtain  $\text{TS} \sim 773.10$  and an average flux of  $(1.06 \pm 0.08) \times 10^{-11}$  erg cm $^{-2}$  s $^{-1}$  with a BPL spectral form in the 0.1–500 GeV energy band. The derived spectral parameters are  $E_b = 2.46 \pm 0.09$  GeV,  $\Gamma_\gamma^1 = 3.25 \pm 0.15$ , and  $\Gamma_\gamma^2 = 1.81 \pm 0.07$ . The fitting parameters are also listed in Table 1.

In order to investigate the  $\gamma$ -ray variability of Pictor A, we generate the  $\sim 16$ -year light curve in the 0.1–500 GeV energy band with a time bin of three months. As shown in Figure 3(a), evident flux variations are presented in the  $\gamma$ -ray light curve. Based on a comparison of these fluxes with the average value, we tentatively identify two periods (F1 and F3) as high-flux states and one period (F2) as a low-flux state for Pictor A. We also calculate the light curves in the 0.1–2.46 GeV band (below the spectral break) and the 2.46–500 GeV band (above the spectral break) using an adaptive-binning method based on a criterion of  $\text{TS} \geq 9$  for each time bin, where the minimum time bin is three months. The results are displayed in Figures 3 (b) and (c). The light curves with different intervals are obtained by freeing the normalization of Pictor A and 4FGL J0515.6–4556 while keeping all other spectral parameters fixed at their best-fit values obtained from the  $\sim 16$ -year data analysis.

## 2.2. IXPE

Pictor A was observed by IXPE from 2024 June 15 to 2024 July 5, with a net exposure of  $\sim 960$  ks. The WHS is the primary target of that IXPE observation. However, the nucleus of Pictor A was also captured within the field of view (FOV) of IXPE, albeit in close proximity to the FOV edge of instrument.

The nucleus and WHS are both identified as point-like sources under a  $\sim 30''$  angular resolution of IXPE. We first apply coordinates correction to publicly available Level-2 event files to remove the detector pointing misalignment. We calculate the X-ray polarization parameters from the IXPE observation using two different methods: (1) the Kislat et al. (2015) method implemented in the PCUBE algorithm within the `xpbin` task of the `ixpeobssim` (v.31.0.1) simulation and analysis software (Baldini et al. 2022) and (2) a spectropolarimetric analysis using `Xspec` (v.12.12.1; Arnaud et al. 1999), which is described in Strohmayer (2017). The source region of the nucleus is defined as a circle with a radius of  $60''$  centered on its radio position. Similarly, the source region for the WHS is also defined as a circle on the Chandra pointing position in Wilson et al. (2001), but with a smaller radius of  $30''$  due to its faintness compared to the nucleus. The background photons for both the nucleus and WHS are extracted from a nearby circle region with a radius of  $90''$ , taking into account the issue of the FOV edge.

The polarization parameters of the nucleus and WHS are first calculated using the PCUBE algorithm within `ixpeobssim` in the 2–8 keV energy range. No significant polarization is observed for either the nucleus or WHS. The analysis with PCUBE yields a minimum detectable polarization at 99% significance ( $\text{MDP}_{99}$ ) of 7.2% for the nucleus based on the three combined IXPE detector units (DUs). However, due to a limited number of detected photons, this estimated  $\text{MDP}_{99}$  value exceeds the theoretical maximum polarization degree of 70%, thereby constraining further investigation into the polarization properties of WHS.

The spectropolarimetric analysis is performed to the nucleus using `Xspec` in the `HEASoft` (v.6.30.1). We generate Stokes parameter spectra ( $I$ ,  $Q$  and  $U$ ) for both the source and background using the `PHA1`, `PHA1Q` and `PHA1U` algorithms within `xpbin`. The  $I$  spectrum is rebinned with a minimum of 20 counts per spectral channel via the `ftgroupppha` task, while a constant energy binning of 0.2 keV is applied to both the  $Q$  and  $U$  spectra. We simultaneously fit the  $I$ ,  $Q$  and  $U$  spectra of three DUs using an absorbed PL model with a constant polarization of the form `CONSTANT`  $\times$  `TBABS`  $\times$  `POLCONST`  $\times$  `POWERLAW`. The PL function is

$$\frac{dN(E)}{dE} = N_0 \times \left(\frac{E}{E_0}\right)^{-\Gamma_x}, \quad (3)$$

where  $E_0 = 1$  keV is the scale parameter of photon energy,  $N_0$  is the PL normalization, and  $\Gamma_x$  is the photon spectral index (Massaro et al. 2004). The `CONSTANT` and `TBABS` models account for the uncertainties in the

absolute effective area of the three DUs and the Galactic photoelectric absorption, respectively. During the spectropolarimetric fit, the column density is fixed to  $N_{\text{H}} = 3.6 \times 10^{20} \text{ cm}^{-2}$  (Gulati et al. 2023). The polarization model POLCONST assumes constant polarization parameters within the operating energy range and has only two free parameters: polarization degree ( $\Pi_{\text{X}}$ ) and polarization angle ( $\psi_{\text{X}}$ ). The best-fit parameters are presented in Table 2.

We further perform an energy-resolved spectropolarimetric analysis on the nucleus following the methodology provided in Errando et al. (2024) and Hu et al. (2024). The results of this analysis are described in section 3.3.

### 3. RESULTS

#### 3.1. Complex $\gamma$ -ray Behaviors of Pictor A

As illustrated in Figure 2(a), the average spectrum of Pictor A over the full time shows a noticeable break at  $2.46 \pm 0.09 \text{ GeV}$ , with the spectral index hardening from  $\Gamma_{\gamma}^1 = 3.25 \pm 0.15$  to  $\Gamma_{\gamma}^2 = 1.81 \pm 0.07$ . The BPL spectral model is preferred over the single PL spectral model for fitting this spectrum at a confidence level of  $5.8\sigma$ . Moreover, both energy bands (0.1–2.46 GeV and 2.46–500 GeV) can be well described by a PL function, yielding photon spectral indices of  $3.12 \pm 0.06$  and  $1.97 \pm 0.18$ , respectively, which are consistent with those obtained from fitting the entire energy band using a BPL model. These results are summarized in Table 1. These findings suggest the presence of statistically significant hardening in the observed  $\gamma$ -ray spectrum of Pictor A, similar to what has been observed in the other two RGs: Cen A (Sahakyan et al. 2013; Brown et al. 2017) and M87 (Ait Benkhali et al. 2019). Such an “unusual” break could most naturally be explained by a superposition of different spectral components. In order to further investigate the properties of GeV emission from Pictor A, additional data analysis on Fermi-LAT observations is conducted and the main findings are summarized below.

- **The full energy light curve.** The derived  $\sim 16$ -year Fermi-LAT light curve of Pictor A in the 0.1–500 GeV band exhibits significant variability, particularly during periods F1 and F3, as illustrated in Figure 3(a). To quantify the variability of the  $\gamma$ -ray light curve, we employ the  $\chi^2$  test (Chen et al. 2022) to the light curve, which yields a probability of  $P(\chi^2) = 6.14 \times 10^{-10}$ , corresponding to a confidence level of  $6.1\sigma$ .
- **The light curves below and above the spectral break.** To investigate the temporal characteristics of the two spectral components, we also

derive the long-term  $\gamma$ -ray light curve of Pictor A above and below the spectral break, i.e., in the 0.1–2.46 GeV and 2.46–500 GeV bands, respectively, as displayed in Figures 3(b) and 3(c). Interestingly, the low-energy light curve exhibits evident flux variability with a probability of  $P(\chi^2) = 1.04 \times 10^{-32}$ , corresponding to a confidence level of  $11.9\sigma$ , while no significant flux variability is observed in the high-energy light curve. This indicates that the dominant statistical contribution to the full energy light curve comes from the low-energy band component.

- **The spectra of low-flux and high-flux states.** The spectrum shown in Figure 2(a) is a  $\sim 16$ -year average spectrum, covering the different flux states of source. We thus extract the time-integrated spectra in the 0.1–500 GeV band for three different stages: MJD 55762–58732 (period F2) for the low-flux state, together with MJD 54952–55762 (period F1) and MJD 58822–59272 (period F3) for the two high-flux states, respectively. As illustrated in Figure 2(b), both spectra from the high-flux states can be well fitted using a PL function; however, they exhibit different spectral indices:  $\Gamma_{\gamma} = 2.59 \pm 0.21$  for F1 state and  $\Gamma_{\gamma} = 3.30 \pm 0.17$  for F3 state. Nonetheless, to account for the low-flux spectrum (F2 state), a BPL function is still necessary ( $\Delta\text{TS} = 11.51$ , corresponding to a significance of  $3.4\sigma$ ), characterized by  $\Gamma_{\gamma}^1 = 3.13 \pm 0.08$ ,  $\Gamma_{\gamma}^2 = 1.92 \pm 0.16$ , and a break energy of  $2.15 \pm 0.27 \text{ GeV}$ .

The aforementioned findings provide support for the idea that the spectrum depicted in Figure 2(a) results from the superposition of two distinct physical components. One component dominates the low-energy band, particularly during periods of high-flux emission, while another component primarily contributes to the high-energy band, which is more prominent during low-flux state of the source. The contrasting variability patterns above and below the spectral break could potentially serve as additional evidence for the existence of these two separate components in the  $\gamma$ -ray emission of Pictor A.

#### 3.2. Possible $\gamma$ -ray Emission from WHS

The analysis results of the Fermi-LAT data clearly indicate that the  $\gamma$ -rays detected from Pictor A have two distinct origins: one component dominates the observed flux and exhibits significant variability, primarily contributing to the emission at low energies (below the spectral break) with a steep spectrum; while another com-



ponent contributes to the high-energy emission (above the spectral break) without evident variability, displaying a hard spectrum. Through broadband SED fitting of the nucleus and WHS in Pictor A, Zhang et al. (2009) proposed that there is detectable  $\gamma$ -ray emission in WHS. The combined spectrum from both the nucleus and WHS in the GeV band would manifest as a BPL feature, with a harder spectrum at higher energy ranges, as illustrated in Figure 3 of their study. Therefore, we suggest that the high-energy component observed above the spectral break in Pictor A is predominantly due to the emission from WHS, while radiation from the nucleus primarily accounts for low-energy emission below this break and exhibits evident variability in Pictor A.

### 3.3. X-Ray Polarization of the nucleus and WHS

By analyzing the observational data from IXPE on Pictor A, only an upper limit of polarization degree is derived for the nucleus, i.e.,  $\Pi_X < 8.9\%$  at a 99% confidence level in the 2–8 keV band. To investigate whether detectable polarization exists within a narrow energy band, we divide the entire energy range of 2–8 keV into energy bins with intervals of 1 keV, 1.5 keV, or 2 keV. Interestingly, the polarization parameters can be estimated with a confidence level exceeding 99% in the energy bands of 5–6 keV, 5–6.5 keV, and 5–7 keV. Based on our spectropolarimetric fitting results at respective confidence levels of  $3.4\sigma$ ,  $3.9\sigma$ , and  $4.0\sigma$ , we find  $\Pi_X = 23.9\% \pm 7.1\%$  with  $\psi_X = 131.1^\circ \pm 8.5^\circ$  in the 5–6 keV band,  $\Pi_X = 23.5\% \pm 6.0\%$  with  $\psi_X = 128.4^\circ \pm 7.3^\circ$  in the 5–6.5 keV band, and  $\Pi_X = 23.5\% \pm 5.6\%$  with  $\psi_X = 131.2^\circ \pm 6.9^\circ$  in the 5–7 keV band. The derived value of  $\psi_X$  is slight larger than the jet position angle, which is about  $100^\circ$  (Perley et al. 1997; Tingay et al. 2000).

The radio (Perley et al. 1997) and optical bands (Roeser & Meisenheimer 1987; Thomson et al. 1995) have detected high polarization in WHS, reaching up to the theoretical maximum of approximately 70%. Furthermore, there is a remarkable similarity in structures between the radio and optical bands. However, due to a limited number of detection photons, no statistical X-ray polarization information can be obtained from this IXPE observation for WHS.

## 4. CONSTRUCTING AND MODELING THE SED

The observed BPL spectral pattern in Pictor A, exhibiting a harder spectrum at higher energy bands, implies the existence of two distinct sources contributing to its  $\gamma$ -ray emission. In order to further investigate the  $\gamma$ -ray emission characteristics of Pictor A, we construct broadband SEDs for both the nucleus and WHS regions,

covering the energy band from radio to  $\gamma$ -rays, as illustrated in Figure 4. The data for both the nucleus and WHS, ranging from radio to X-rays, are obtained from Gulati et al. (2023) and references therein (for more details, please refer to the caption of Figure 4), while the  $\gamma$ -ray spectrum is derived through our own analysis in this study. As described in Section 3, the low-energy and high-energy components are proposed to primarily originate from the nucleus and WHS, respectively. The results appear to be consistent with their broadband SEDs, as shown in Figure 4; the combinations with their respective radio to X-ray data result in smooth features in their broadband SEDs.

The leptonic model is commonly used to fit the broadband SEDs of the jet emission from AGNs. The radiation region is assumed to be a sphere with a radius  $R$ , magnetic field strength  $B$ , the bulk Lorentz factor  $\Gamma$ , and the Doppler boosting factor  $\delta$ . The electron distribution in the emission region is taken as a PL or a BPL, characterized by an electron density parameter ( $N_0$ ), a break energy ( $\gamma_b$ ), and indices ( $p_1$  and  $p_2$ ) ranging from  $\gamma_{\min}$  to  $\gamma_{\max}$ . In the case of a PL electron distribution,  $p_1 = p_2$  and  $\gamma_b = \gamma_{\max}$ . Additionally, the synchrotron-self absorption, Klein–Nishina effect, and extragalactic background light absorption (Finke et al. 2022) are considered during the SED modeling.

### 4.1. Nucleus Region

The synchrotron and SSC processes of relativistic electrons with a BPL distribution are commonly used to explain the observed SED of the nucleus in  $\gamma$ -ray emitting RGs (Abdo et al. 2009; Migliori et al. 2011; Fukazawa et al. 2015; Xue et al. 2017; Yu et al. 2024), which is also used to represent the observed SED of the nucleus in Pictor A. The emission region radius is fixed at  $R = 10^{16}$  cm, as also mentioned in Zhang et al. (2009) and Gulati et al. (2023). We adopt  $\Gamma = 5$  with a viewing angle of  $30^\circ$  (Gulati et al. 2023), corresponding to  $\delta = 1.3$ . The values of  $p_1$  and  $p_2$  are determined using the observed spectral indices in X-rays and optical–UV bands, respectively. We set  $\gamma_{\min} = 1$ , while  $\gamma_{\max}$  is approximately constrained by the observed GeV spectrum, showing a cutoff at the break frequency. By adjusting the parameters  $B$ ,  $N_0$ , and  $\gamma_b$  to match the broadband SED of the nucleus, we obtain  $B = 7$  G,  $\gamma_b = 1.6 \times 10^3$ , and  $\gamma_{\max} = 1.6 \times 10^4$ . The modeling parameters are also listed in Table 3.

The fitting result is presented in Figure 4; the one-zone synchrotron+SSC model well represents the broadband SED of the nucleus. It is evident that this model fails to account for the high-energy component observed in the Fermi-LAT spectrum, even without considering the low-

energy component of the  $\gamma$ -ray spectrum. If the high-energy component also stems from the inner jet of Pictor A, a more complex radiation model is required to reproduce the observed broadband SED of nucleus, such as a spine-layer model (Tavecchio & Ghisellini 2008) or hadronic processes (e.g., Cheng et al. 2022).

It should be noted that there exists a degeneracy between  $B$  and  $\delta$  during the SED modeling process (e.g., Zhang et al. 2012). Taking a similar value of  $R \sim 10^{16}$  cm, Gulati et al. (2023) reported  $\delta = 1.3$  with  $B = 10$  G, whereas Zhang et al. (2009) found  $\delta = 1.6$  with  $B = 7$  G, and Xue et al. (2017) obtained  $\delta = 2.5$  with  $B = 4.2$  G. Considering the dominance of the low-energy component in the high-flux  $\gamma$ -ray emission state of Pictor A, as illustrated in Figure 2(b), the X-ray spectrum obtained during the high-flux state Gulati et al. (2023) into account in our SED modeling. Consequently, the obtained value of  $B$  differs from theirs due to the different X-ray and  $\gamma$ -ray data.

#### 4.2. WHS

Considering the complex radio structure (Perley et al. 1997; Tingay et al. 2008) and flat X-ray spectrum of WHS (e.g., Zhang et al. 2009; Gulati et al. 2023), we use a two-zone leptonic model to fit its broadband SED from radio to X-rays, same model as taken in Zhang et al. (2009) and Gulati et al. (2023). This model includes synchrotron and SSC radiations originating from both a diffuse region and a compact substructure, where both regions are treated as stationary blobs characterized by  $\Gamma = \delta = 1$ . The energy density of the synchrotron radiation field in this scenario surpasses that of the cosmic microwave background (CMB) by more than one order of magnitude. Consequently, the contribution of the inverse Compton scattering of CMB photons by relativistic electrons can be considered negligible when compared to the SSC process. The emission of WHS from radio, optical to ultraviolet is primarily attributed to the synchrotron process occurring in the whole diffuse region, while the X-rays are produced through synchrotron radiation emitted by a compact substructure contained within the diffuse region. The  $\gamma$ -ray spectrum above the break in Figure 2(a) is taken into consideration in the SED modeling of the WHS.

For the diffuse region of WHS, a radius of  $R = 500$  pc is adopted, which corresponds to half of the overall size (1.4 arcsec, Thomson et al. 1995) of WHS in the optical band. The electron distribution follows a BPL, with  $p_1$  and  $p_2$  being well constrained by observed data across radio to UV bands.  $\gamma_{\min}$  cannot be determined and is fixed at 1, while  $\gamma_{\max}$  is roughly constrained by the last data point in the UV band. Considering the equipar-

tion condition ( $U_B = U_e$ ), where  $U_B$  and  $U_e$  are the energy densities of the magnetic fields and electrons in the radiation region, it is found that the prediction flux from SSC process fails to explain the  $\gamma$ -ray spectrum at GeV energies. The fitting of the highest-energy point in the GeV band necessitates a significantly small magnetic field that deviates substantially from the equipartition condition, while also resulting in the model's prediction line surpassing the two data points above the break. Therefore, we abandon this hypothesis.

For the compact substructure of WHS, a radius of  $R = 30$  pc is taken, which is half the average size of the five compact substructures reported by Tingay et al. (2008). Considering the limited observational data, we adopt a PL electron distribution.  $p_1$  is determined based on the spectral index between radio and soft X-rays.  $\gamma_{\min}$  is also fixed at 1. When considering equipartition conditions, the predicted line from the SSC process is significantly lower than the  $\gamma$ -ray fluxes observed at the GeV band, similar to that of the diffuse region. We propose that the  $\gamma$ -rays primarily originate from the compact substructure; therefore, the equipartition condition in the compact substructure is not taken into account during SED modeling of WHS.

We adjust the values of  $N_0$  and  $\gamma_b$  for the diffuse region under the equipartition condition, along with adjusting the parameters  $N_0$ ,  $B$ , and  $\gamma_{\max}$  of the compact substructure to represent the observed SED of WHS from radio to  $\gamma$ -ray bands. The fitting result is presented in Figure 4 and the parameters are given in Table 3. The parameter values for the diffuse region are found to be similar when compared with those in Gulati et al. (2023). However, the  $B$  value for the compact substructure is one order of magnitude smaller, accompanied by a slightly higher value of  $\gamma_{\max}$  in order to match the  $\gamma$ -ray spectrum. Additionally, we observe that the predicted flux of SED modeling is over the sensitivity curve of Cherenkov Telescope Array (CTA) south array (CTA-S, 50 hr), but remains below the sensitivity of High Energy Stereoscopic System (H.E.S.S.), where the sensitivity curves are obtained from Wang et al. (2022) and the CTA webpage<sup>3</sup>, respectively. Considering the hard spectrum in the GeV band, it could potentially be considered as a candidate for CTA.

## 5. DISCUSSION AND CONCLUSIONS

By analyzing the Fermi-LAT observation data, we find that the  $\sim 16$ -year average spectrum of Pictor A in the GeV band exhibits statistically significant hard-

<sup>3</sup> <https://www.ctao.org/for-scientists/performance/>

ening feature. The BPL spectral form is more preferred than a simple PL function for describing the  $\gamma$ -ray spectrum of Pictor A with a confidence level of  $5.8\sigma$ . Similar behavior featuring significant hardening in the GeV  $\gamma$ -ray spectrum has also been observed in two other RGs: Cen A (Sahakyan et al. 2013; Brown et al. 2017) and M 87 (Ait Benkhali et al. 2019). In both cases, it was proposed that the GeV emission consists of two distinct physical components. For M 87, the hardening  $\gamma$ -ray spectrum was observed at a significance level of  $\sim 2.66\sigma$ , and both components were suggested to stem from the inner jet (Ait Benkhali et al. 2019). For Cen A, the significance level of the hardening  $\gamma$ -ray spectrum increased from  $2.3\sigma$  (Sahakyan et al. 2013) based on the 4-year Fermi-LAT observation data to  $> 5\sigma$  (Brown et al. 2017) when utilizing the 8-year Fermi-LAT observation data. They suggested that this additional high-energy component beyond the common SSC emission may be related with the interactions between relativistic protons and ambient gas in the large-scale jet (Sahakyan et al. 2013), or the dark matter around the black hole, or a population of millisecond pulsars in the core region (Brown et al. 2017).

The dominant low-energy component with a steep spectrum, which exhibits significant variability and accounts for the majority of the emission flux in Pictor A, is likely to originate from its nucleus. Contrarily, the high-energy component with a hard spectrum remains in a steady emission state, which is favored by the extended  $\gamma$ -ray production scenario. We propose that this high-energy component stems from the WHS and that the observed BPL spectrum in the GeV band of Pictor A results from the combined emission originating from both its nucleus and WHS.

We use a single-zone leptonic model to explain the broadband SED of the nucleus, while adopting a two-zone leptonic model to represent the broadband SED of WHS. The two components in the GeV spectrum of Pictor A smoothly connect with the X-ray spectra of the nucleus and WHS, respectively; both can be naturally represented by the SSC process occurring in two different regions. Moreover, our SED fitting predicts that CTA-S will be able to detect very high energy (VHE) emission from WHS. Notably, H.E.S.S. observations have unveiled VHE  $\gamma$ -ray emission along the large-scale jet of RG Cen A (H. E. S. S. Collaboration et al. 2020), providing compelling evidence supporting large-scale jets as sites for accelerating ultrarelativistic electrons.

By analyzing the first IXPE observation data for Pictor A, we obtain an upper limit ( $< 8.9\%$ ) for the polarization degree of the nucleus at a 99% confidence level. This finding is consistent with the low-

polarization expectation that the X-ray emission of the nucleus is produced by the SSC process (Krawczynski 2012; Peirson & Romani 2019), similar to the IXPE observation results of RG Cen A (Ehlert et al. 2022) and other low and intermediate spectral peak blazars (Marshall et al. 2023). We also note that the nucleus of Pictor A generally exhibits low polarization in the radio band, typically less than 5% (Perley et al. 1997 and references therein). However, no optical polarimetry data is available in the archived records.

Although no significant polarization is detected in the 2–8 keV band for the nucleus, a polarization degree of  $23.5\% \pm 5.6\%$  is observed at a confidence level exceeding 99% in the 5–7 keV band. As described in Section 2.2, the X-ray spectrum of the nucleus can be adequately explained by a simple PL function. This is also consistent with recent studies employing other X-ray detectors (e.g., Sunada et al. 2022; Gulati et al. 2023). It is implausible that this narrow-energy-band polarization arises from superimposed components originating from other regions or radiation processes. The presence of a weak Fe K $\alpha$  line with an energy of  $6.36 \pm 0.02$  keV has been reported in the X-ray spectrum of the nucleus by Hardcastle et al. (2016). Hence, we speculate that this polarization signal may be associated with this emission line; however, Ursini et al. (2023) suggested that the absence of significant polarization detection for Circinus galaxy in the 6–8 keV band is likely due to the prominent iron lines present in its spectrum. The confidence level of this narrow-energy-band polarization signal in Pictor A is no greater than  $5\sigma$ , therefore, we suggest that it represents a tentative detection.

Additionally, numerous studies have suggested that the X-rays emitted by WHS originate from synchrotron radiation within a compact substructure (Wilson et al. 2001; Tingay et al. 2008; Zhang et al. 2009; Hardcastle et al. 2016; Gulati et al. 2023). Considering the significant polarization observed in both radio and optical bands, with some measurements reaching up to the theoretical maximum of approximately 70% (Roesser & Meisenheimer 1987; Thomson et al. 1995; Perley et al. 1997), it is expected that high polarization detection of WHS in the X-ray band, which would provide a valuable tool for investigating radiation mechanisms of X-rays in WHS. Unfortunately, due to the limited number of detected photons, this IXPE observation is unable to provide any statistical polarization information for WHS.

<sup>1</sup> This work is supported by the National Key R&D  
<sup>2</sup> Program of China (grant 2023YFE0117200) and the  
<sup>3</sup> National Natural Science Foundation of China (grants  
<sup>4</sup> 12203022, 12022305, and 11973050).



## REFERENCES

- Abdo, A. A., Ackermann, M., Ajello, M., et al. 2009, *ApJ*, 707, 55, doi: [10.1088/0004-637X/707/1/55](https://doi.org/10.1088/0004-637X/707/1/55)
- . 2010, *ApJ*, 719, 1433, doi: [10.1088/0004-637X/719/2/1433](https://doi.org/10.1088/0004-637X/719/2/1433)
- Abdollahi, S., Acero, F., Ackermann, M., et al. 2020, *ApJS*, 247, 33, doi: [10.3847/1538-4365/ab6bcb](https://doi.org/10.3847/1538-4365/ab6bcb)
- Abdollahi, S., Acero, F., Baldini, L., et al. 2022, *ApJS*, 260, 53, doi: [10.3847/1538-4365/ac6751](https://doi.org/10.3847/1538-4365/ac6751)
- Ackermann, M., Ajello, M., Baldini, L., et al. 2016, *ApJ*, 826, 1, doi: [10.3847/0004-637X/826/1/1](https://doi.org/10.3847/0004-637X/826/1/1)
- Ait Benkhali, F., Chakraborty, N., & Rieger, F. M. 2019, *A&A*, 623, A2, doi: [10.1051/0004-6361/201732334](https://doi.org/10.1051/0004-6361/201732334)
- Arnaud, K., Dorman, B., & Gordon, C. 1999, XSPEC: An X-ray spectral fitting package, Astrophysics Source Code Library, record ascl:9910.005. <http://ascl.net/9910.005>
- Baldini, L., Bucciantini, N., Lalla, N. D., et al. 2022, *SoftwareX*, 19, 101194, doi: [10.1016/j.softx.2022.101194](https://doi.org/10.1016/j.softx.2022.101194)
- Ballet, J., Bruel, P., Burnett, T. H., Lott, B., & The Fermi-LAT collaboration. 2023, arXiv e-prints, arXiv:2307.12546, doi: [10.48550/arXiv.2307.12546](https://doi.org/10.48550/arXiv.2307.12546)
- Brown, A. M., & Adams, J. 2012, *MNRAS*, 421, 2303, doi: [10.1111/j.1365-2966.2012.20451.x](https://doi.org/10.1111/j.1365-2966.2012.20451.x)
- Brown, A. M., BÅhm, C., Graham, J., et al. 2017, *PhRvD*, 95, 063018, doi: [10.1103/PhysRevD.95.063018](https://doi.org/10.1103/PhysRevD.95.063018)
- Chen, S., Laor, A., & Behar, E. 2022, *MNRAS*, 515, 1723, doi: [10.1093/mnras/stac1891](https://doi.org/10.1093/mnras/stac1891)
- Cheng, J.-G., Huang, X.-L., Wang, Z.-R., Huang, J.-K., & Liang, E.-W. 2022, *ApJL*, 925, L19, doi: [10.3847/2041-8213/ac4d8e](https://doi.org/10.3847/2041-8213/ac4d8e)
- Cutri, R. M., Wright, E. L., Conrow, T., et al. 2013, Explanatory Supplement to the AllWISE Data Release Products, Explanatory Supplement to the AllWISE Data Release Products, by R. M. Cutri et al.
- Ehlert, S. R., Ferrazzoli, R., Marinucci, A., et al. 2022, *ApJ*, 935, 116, doi: [10.3847/1538-4357/ac8056](https://doi.org/10.3847/1538-4357/ac8056)
- Eracleous, M., & Halpern, J. P. 1998, *ApJ*, 505, 577, doi: [10.1086/306190](https://doi.org/10.1086/306190)
- Errando, M., Liodakis, I., Marscher, A. P., et al. 2024, *ApJ*, 963, 5, doi: [10.3847/1538-4357/ad1ce4](https://doi.org/10.3847/1538-4357/ad1ce4)
- Finke, J. D., Ajello, M., Domínguez, A., et al. 2022, *ApJ*, 941, 33, doi: [10.3847/1538-4357/ac9843](https://doi.org/10.3847/1538-4357/ac9843)
- Fukazawa, Y., Finke, J., Stawarz, L., et al. 2015, *ApJ*, 798, 74, doi: [10.1088/0004-637X/798/2/74](https://doi.org/10.1088/0004-637X/798/2/74)
- Gulati, S., Bhattacharya, D., Ramadevi, M. C., Stalin, C. S., & Sreekumar, P. 2023, *MNRAS*, 521, 2704, doi: [10.1093/mnras/stad716](https://doi.org/10.1093/mnras/stad716)
- Guo, S.-C., Zhang, H.-M., Zhang, J., & Liang, E.-W. 2018, *Research in Astronomy and Astrophysics*, 18, 070, doi: [10.1088/1674-4527/18/6/70](https://doi.org/10.1088/1674-4527/18/6/70)
- H. E. S. S. Collaboration, Abdalla, H., Adam, R., et al. 2020, *Nature*, 582, 356, doi: [10.1038/s41586-020-2354-1](https://doi.org/10.1038/s41586-020-2354-1)
- Hardcastle, M. J., Lenc, E., Birkinshaw, M., et al. 2016, *MNRAS*, 455, 3526, doi: [10.1093/mnras/stv2553](https://doi.org/10.1093/mnras/stv2553)
- Harris, D. E., & Krawczynski, H. 2006, *ARA&A*, 44, 463, doi: [10.1146/annurev.astro.44.051905.092446](https://doi.org/10.1146/annurev.astro.44.051905.092446)
- He, J.-C., Sun, X.-N., Wang, J.-S., et al. 2023, *MNRAS*, 525, 5298, doi: [10.1093/mnras/stad2542](https://doi.org/10.1093/mnras/stad2542)
- Hu, X.-K., Yu, Y.-W., Zhang, J., et al. 2024, arXiv e-prints, arXiv:2402.11949, doi: [10.48550/arXiv.2402.11949](https://doi.org/10.48550/arXiv.2402.11949)
- Isobe, N., Koyama, S., Kino, M., et al. 2017, *ApJ*, 850, 193, doi: [10.3847/1538-4357/aa94c9](https://doi.org/10.3847/1538-4357/aa94c9)
- Isobe, N., Sunada, Y., Kino, M., et al. 2020, *ApJ*, 899, 17, doi: [10.3847/1538-4357/ab9d1c](https://doi.org/10.3847/1538-4357/ab9d1c)
- Kataoka, J., & Stawarz, L. 2005, *ApJ*, 622, 797, doi: [10.1086/428083](https://doi.org/10.1086/428083)
- Kislat, F., Clark, B., Beilicke, M., & Krawczynski, H. 2015, *Astroparticle Physics*, 68, 45, doi: [10.1016/j.astropartphys.2015.02.007](https://doi.org/10.1016/j.astropartphys.2015.02.007)
- Krawczynski, H. 2012, *ApJ*, 744, 30, doi: [10.1088/0004-637X/744/1/30](https://doi.org/10.1088/0004-637X/744/1/30)
- Marshall, H. L., Liodakis, I., Marscher, A. P., et al. 2023, arXiv e-prints, arXiv:2310.11510, doi: [10.48550/arXiv.2310.11510](https://doi.org/10.48550/arXiv.2310.11510)
- Massaro, E., Perri, M., Giommi, P., & Nesci, R. 2004, *A&A*, 413, 489, doi: [10.1051/0004-6361:20031558](https://doi.org/10.1051/0004-6361:20031558)
- Meisenheimer, K., Roser, H. J., Hiltner, P. R., et al. 1989, *A&A*, 219, 63
- Meisenheimer, K., Yates, M. G., & Roeser, H. J. 1997, *A&A*, 325, 57
- Migliori, G., Grandi, P., Torresi, E., et al. 2011, *A&A*, 533, A72, doi: [10.1051/0004-6361/201116808](https://doi.org/10.1051/0004-6361/201116808)
- Peirson, A. L., & Romani, R. W. 2019, *ApJ*, 885, 76, doi: [10.3847/1538-4357/ab46b1](https://doi.org/10.3847/1538-4357/ab46b1)
- Perley, R. A., Roser, H.-J., & Meisenheimer, K. 1997, *A&A*, 328, 12
- Roeser, H.-J., & Meisenheimer, K. 1987, *ApJ*, 314, 70, doi: [10.1086/165039](https://doi.org/10.1086/165039)
- Sahakyan, N., Yang, R., Aharonian, F. A., & Rieger, F. M. 2013, *ApJL*, 770, L6, doi: [10.1088/2041-8205/770/1/L6](https://doi.org/10.1088/2041-8205/770/1/L6)
- Sambruna, R. M., Eracleous, M., & Mushotzky, R. F. 1999, *ApJ*, 526, 60, doi: [10.1086/307981](https://doi.org/10.1086/307981)
- Schmidt, M. 1965, *ApJ*, 141, 1, doi: [10.1086/148085](https://doi.org/10.1086/148085)
- Shaik, A., Meyer, E. T., Reddy, K., Laha, S., & Georganopoulos, M. 2024, arXiv e-prints, arXiv:2402.06218, doi: [10.48550/arXiv.2402.06218](https://doi.org/10.48550/arXiv.2402.06218)
- Simkin, S. M., Sadler, E. M., Sault, R., Tingay, S. J., & Callcut, J. 1999, *ApJS*, 123, 447, doi: [10.1086/313243](https://doi.org/10.1086/313243)

- Singh, K. P., Rao, A. R., & Vahia, M. N. 1990, MNRAS, 246, 706
- Strohmayer, T. E. 2017, ApJ, 838, 72, doi: [10.3847/1538-4357/aa643d](https://doi.org/10.3847/1538-4357/aa643d)
- Sun, X.-n., Yang, R.-z., Mckinley, B., & Aharonian, F. 2016, A&A, 595, A29, doi: [10.1051/0004-6361/201629069](https://doi.org/10.1051/0004-6361/201629069)
- Sunada, Y., Morimoto, A., Tashiro, M. S., et al. 2022, PASJ, 74, 602, doi: [10.1093/pasj/psac022](https://doi.org/10.1093/pasj/psac022)
- Tavecchio, F., & Ghisellini, G. 2008, MNRAS, 385, L98, doi: [10.1111/j.1745-3933.2008.00441.x](https://doi.org/10.1111/j.1745-3933.2008.00441.x)
- Thimmappa, R., Stawarz, L., Marchenko, V., et al. 2020, ApJ, 903, 109, doi: [10.3847/1538-4357/abb605](https://doi.org/10.3847/1538-4357/abb605)
- Thimmappa, R., Stawarz, L., Neilsen, J., Ostrowski, M., & Reville, B. 2022, ApJ, 941, 204, doi: [10.3847/1538-4357/aca472](https://doi.org/10.3847/1538-4357/aca472)
- Thomson, R. C., Crane, P., & Mackay, C. D. 1995, ApJL, 446, L93, doi: [10.1086/187938](https://doi.org/10.1086/187938)
- Tingay, S. J., Lenc, E., Brunetti, G., & Bondi, M. 2008, AJ, 136, 2473, doi: [10.1088/0004-6256/136/6/2473](https://doi.org/10.1088/0004-6256/136/6/2473)
- Tingay, S. J., Jauncey, D. L., Reynolds, J. E., et al. 2000, AJ, 119, 1695, doi: [10.1086/301283](https://doi.org/10.1086/301283)
- Ursini, F., Marinucci, A., Matt, G., et al. 2023, MNRAS, 519, 50, doi: [10.1093/mnras/stac3189](https://doi.org/10.1093/mnras/stac3189)
- Wang, X.-Y., Bi, X.-J., Cao, Z., et al. 2022, Chinese Physics C, 46, 030003, doi: [10.1088/1674-1137/ac3fa9](https://doi.org/10.1088/1674-1137/ac3fa9)
- Wang, Z.-J., Zhang, J., Sun, X.-N., & Liang, E.-W. 2020, ApJ, 893, 41, doi: [10.3847/1538-4357/ab7d35](https://doi.org/10.3847/1538-4357/ab7d35)
- Weisskopf, M. 2022, in AAS/High Energy Astrophysics Division, Vol. 54, AAS/High Energy Astrophysics Division, 301.01
- Wilson, A. S., Young, A. J., & Shopbell, P. L. 2001, ApJ, 547, 740, doi: [10.1086/318412](https://doi.org/10.1086/318412)
- Wood, M., Caputo, R., Charles, E., et al. 2017, in International Cosmic Ray Conference, Vol. 301, 35th International Cosmic Ray Conference (ICRC2017), 824, doi: [10.22323/1.301.0824](https://doi.org/10.22323/1.301.0824)
- Wright, E. L., Eisenhardt, P. R. M., Mainzer, A. K., et al. 2010, AJ, 140, 1868, doi: [10.1088/0004-6256/140/6/1868](https://doi.org/10.1088/0004-6256/140/6/1868)
- Xue, Z.-W., Zhang, J., Cui, W., Liang, E.-W., & Zhang, S.-N. 2017, Research in Astronomy and Astrophysics, 17, 090, doi: [10.1088/1674-4527/17/9/90](https://doi.org/10.1088/1674-4527/17/9/90)
- Yu, Y.-W., Zhang, H.-M., Gan, Y.-Y., et al. 2024, ApJ, 965, 163, doi: [10.3847/1538-4357/ad2e07](https://doi.org/10.3847/1538-4357/ad2e07)
- Zhang, J., Bai, J. M., Chen, L., & Liang, E. 2010, ApJ, 710, 1017, doi: [10.1088/0004-637X/710/2/1017](https://doi.org/10.1088/0004-637X/710/2/1017)
- Zhang, J., Bai, J. M., Chen, L., & Yang, X. 2009, ApJ, 701, 423, doi: [10.1088/0004-637X/701/1/423](https://doi.org/10.1088/0004-637X/701/1/423)
- Zhang, J., Du, S.-s., Guo, S.-C., et al. 2018, ApJ, 858, 27, doi: [10.3847/1538-4357/aab9b2](https://doi.org/10.3847/1538-4357/aab9b2)
- Zhang, J., Liang, E.-W., Zhang, S.-N., & Bai, J. M. 2012, ApJ, 752, 157, doi: [10.1088/0004-637X/752/2/157](https://doi.org/10.1088/0004-637X/752/2/157)

**Table 1.** Spectral Fitting Results of Fermi-LAT Observations for Pictor A

Time range (MJD)	Energy range (GeV)	Model	$\Gamma_\gamma^1$	$\Gamma_\gamma^2$	$E_b$ (GeV)	Flux ( $\times 10^{-12} \text{ erg cm}^{-2} \text{ s}^{-1}$ )	TS
Full time (54682–60501)	0.1–500	PL	$3.05 \pm 0.08$	–	–	$8.98 \pm 0.73$	669.55
	0.1–500	BPL	$3.25 \pm 0.15$	$1.81 \pm 0.07$	$2.46 \pm 0.09$	$10.61 \pm 0.82$	773.10
	0.1–2.46	PL	$3.12 \pm 0.06$	–	–	$7.68 \pm 0.82$	541.21
	2.46–500	PL	$1.97 \pm 0.18$	–	–	$1.72 \pm 0.56$	64.06
F1 (54952–55762)	0.1–500	PL	$2.59 \pm 0.21$	–	–	$5.91 \pm 1.56$	50.95
F2 (55762–58732)	0.1–500	BPL	$3.13 \pm 0.08$	$1.92 \pm 0.16$	$2.15 \pm 0.27$	$8.47 \pm 1.05$	241.27
F3 (58822–59272)	0.1–500	PL	$3.30 \pm 0.17$	–	–	$16.34 \pm 2.87$	156.39

**Table 2.** Results of the Spectropolarimetric Analysis in the 2–8 keV Band for the Nucleus

Model	Parameter	Value
CONSTANT	$C_{\text{DU1}}$	1.0 (fixed)
	$C_{\text{DU2}}$	$0.995 \pm 0.008$
	$C_{\text{DU3}}$	$0.944 \pm 0.008$
TBABS	$N_{\text{H}}$ ( $10^{20} \text{ cm}^{-2}$ )	3.6 (fixed)
POLCONST	$\Pi_{\text{X}}$ (%)	< 8.9%
	$\psi_{\text{X}}$ ( $^\circ$ )	...
POWERLAW	$\Gamma_{\text{X}}$	$1.86 \pm 0.01$
	Norm ( $10^{-3} \text{ photon keV}^{-1} \text{ cm}^{-2} \text{ s}^{-1}$ )	$5.09 \pm 0.07$
		$\chi^2/\text{dof} = 580/546 = 1.06$

**Table 3.** Parameters of SED Fitting for both the Nucleus and WHS

Parameter	Symbol	Nucleus	WHS	
			Diffuse	Substructure
Electron density parameter	$N_0$ [ $\text{cm}^{-3}$ ]	$6.5 \times 10^5$	$2.6 \times 10^{-3}$	49
Spectral index below break	$p_1^*$	2.2	2.4	2.52
Spectral index above break	$p_2^*$	4.42	4.1	
Minimum electron Lorentz factor	$\gamma_{\text{min}}^*$	1	1	1
Break Lorentz factor	$\gamma_{\text{b}}$	$1.6 \times 10^3$	$2.2 \times 10^5$	
Maximum electron Lorentz factor	$\gamma_{\text{max}}$	$1.6 \times 10^4$	$2.2 \times 10^6$	$2.1 \times 10^8$
Radius of the blob	$R^*$ [cm/pc]	$10^{16} \text{ cm}$	500 pc	30 pc
Bulk Lorentz factor	$\Gamma^*$	5	1	1
Doppler boosting factor	$\delta^*$	1.3	1	1
Magnetic Field	$B$ [G]	7	$3.6 \times 10^{-4}$	$3.5 \times 10^{-5}$
Equipartition ratio	$U_e/U_B$	1.08	1	$1.6 \times 10^6$

\*The parameters remain fixed during SED modeling.

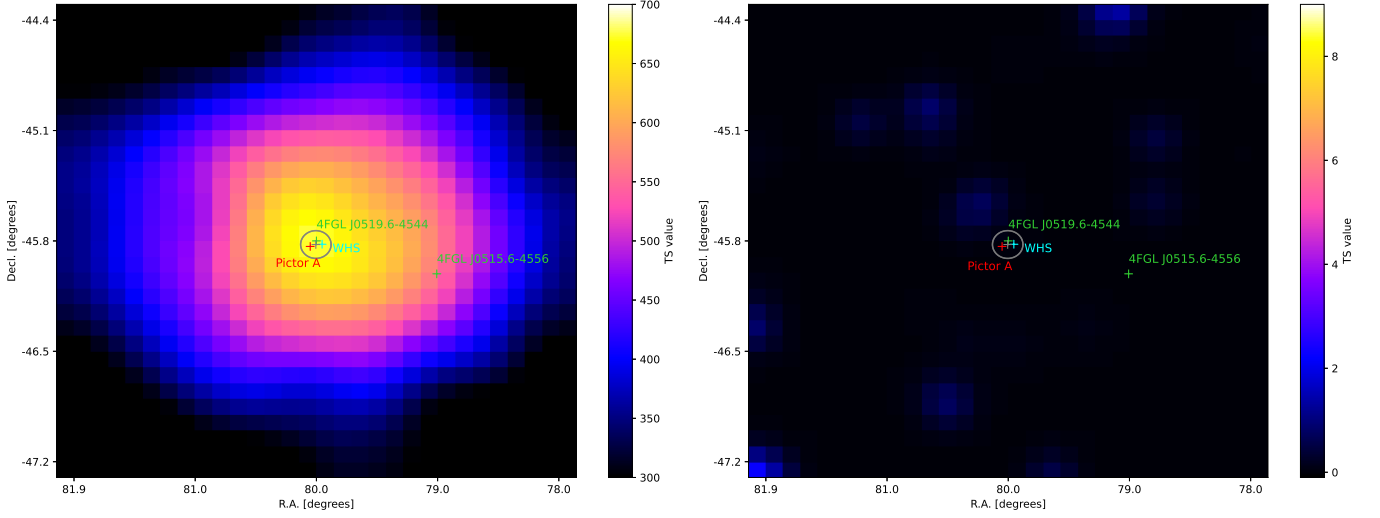


**Figure 1.**  $3^\circ \times 3^\circ$  TS map (left panel) and residual TS map (right panel) of Pictor A in the 0.1–500 GeV band. The green crosses represent the positions of 4FGL J0519.6-4544 and 4FGL J0515.6-4556 in the 4FGL-DR4. The red and cyan crosses represent the radio position of Pictor A and the position of WHS, respectively. The grey cross represents the best-fit position of  $\gamma$ -ray source in this work along with its corresponding 95% containment region.

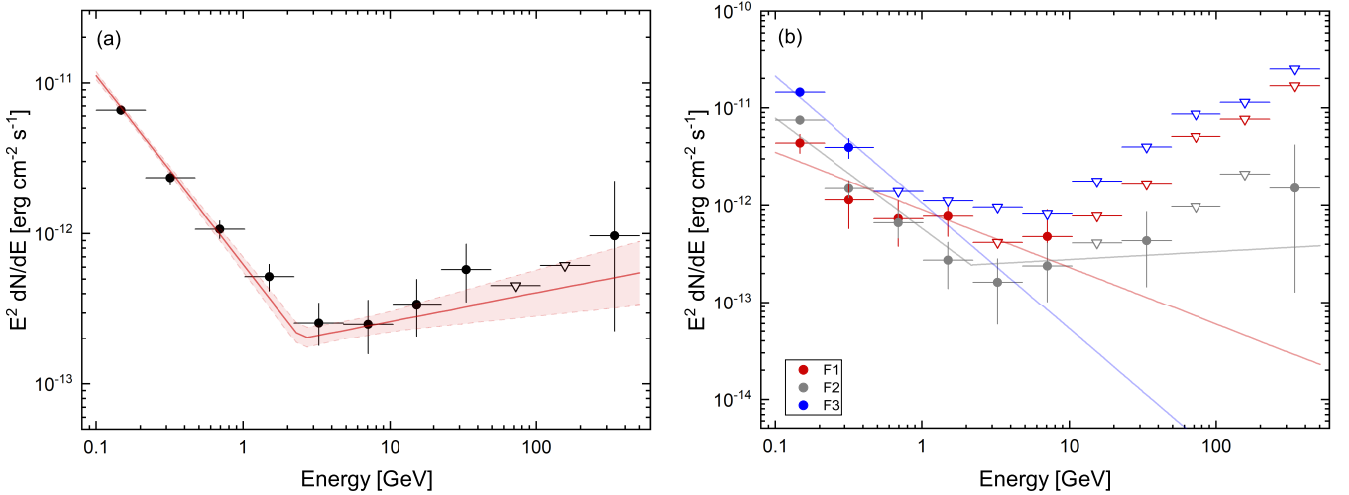


**Figure 2.** The spectra observed by Fermi-LAT for Pictor A in the 0.1–500 GeV band, including the  $\sim 16$ -year average spectrum (Panel (a)) and the spectra of three high/low-states (Panel (b)), corresponding to the three regions shaded in different colors in Figure 3(a). The  $2\sigma$  upper limit (opened inverted triangle) is reported when  $TS \leq 4$  for that energy bin. The color lines represent the corresponding best-fit results using either a BPL or a PL function. The pink shaded region in Panel (a) indicates the  $1\sigma$  uncertainty of fitting result.

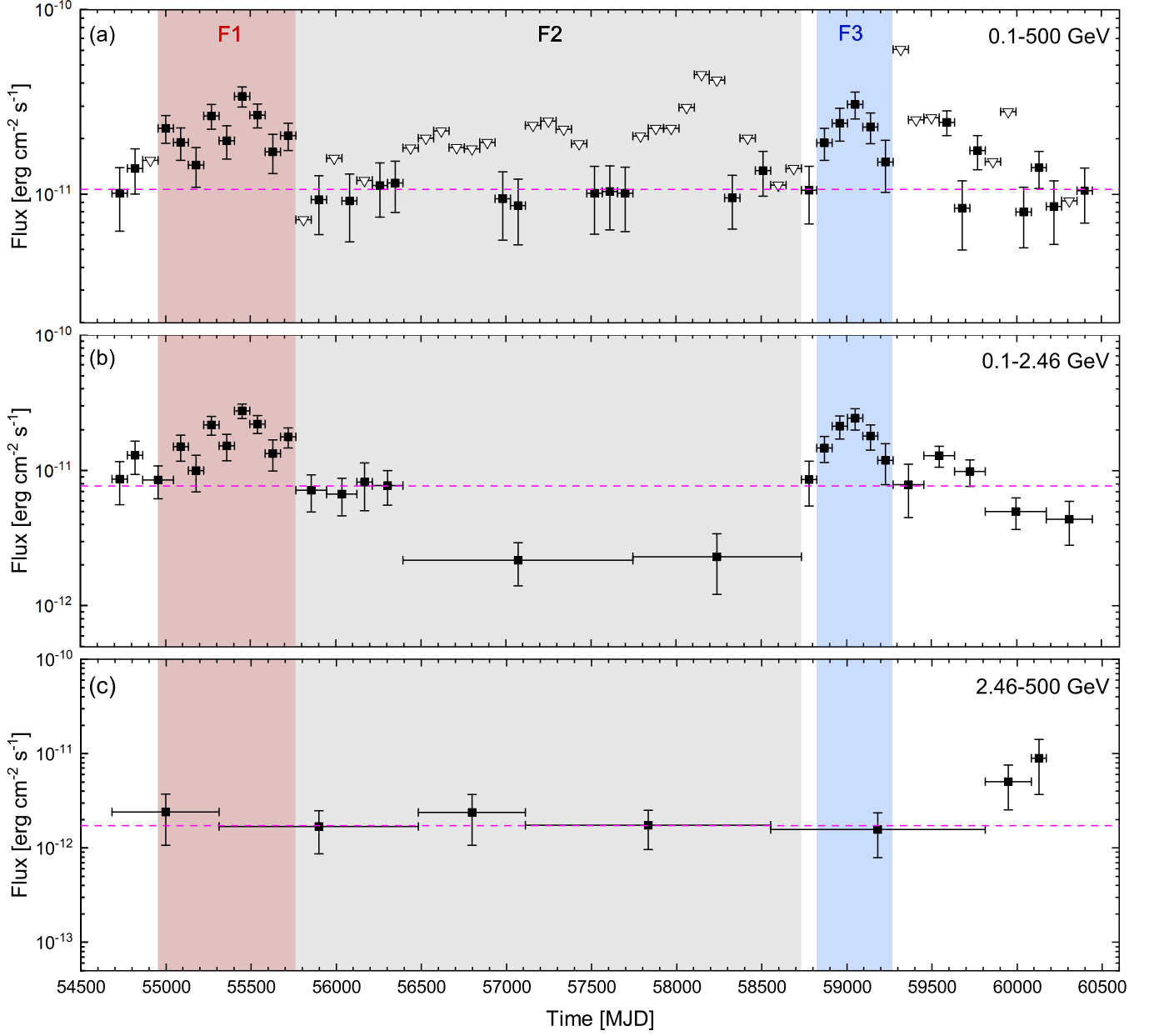


**Figure 3.** The long-term light curves of Pictor A, derived with the  $\sim 16$ -year Fermi-LAT observation data in different energy bands, including the 0.1–500 GeV band (Panel (a)) together with the energy bands below (0.1–2.46 GeV in Panel (b)) and above (2.46–500 GeV in Panel (c)) the spectral break. The horizontal magenta dashed lines represent the average flux in that energy band. In panel (a), each time bin is 3 months, the  $2\sigma$  upper limit is reported when  $TS \leq 9$ . In panels (b) and (c), the light curves are derived with an adaptive-binning method based on a criterion of  $TS \geq 9$  for each time bin, where the minimum time-bin is 3 months.



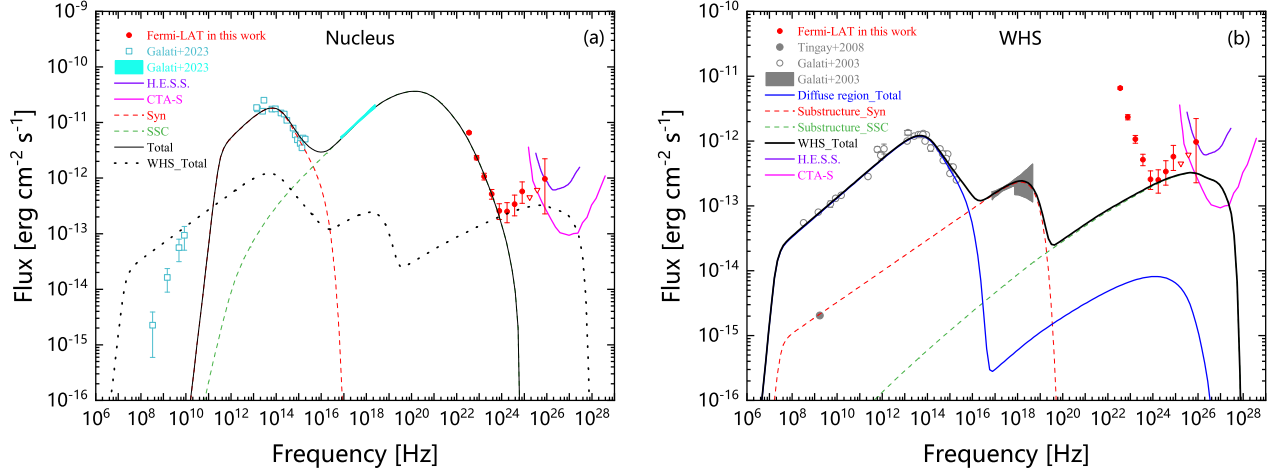


**Figure 4.** Observed SEDs with model fitting for the nucleus (Panel (a)) and the WHS (Panel (b)) in Pictor A. The data from radio to X-rays for both the nucleus and WHS are taken from [Gulati et al. \(2023\)](#) and the references therein; for the WHS, including the radio and optical data from [Meisenheimer et al. \(1997\)](#), the IR and the substructure data from [Tingay et al. \(2008\)](#), the mid-infrared data from [Isobe et al. \(2017\)](#), two optical/near-ultraviolet points from [Wilson et al. \(2001\)](#), the far-infrared data from [Isobe et al. \(2020\)](#), and the NuSTAR spectrum from [Sunada et al. \(2022\)](#); for the nucleus, including the radio data from [Perley et al. \(1997\)](#), the IR data from [Singh et al. \(1990\)](#), and the mid-infrared data from ([Wright et al. 2010](#); [Cutri et al. 2013](#)). It should be noted that this work takes into consideration the X-ray spectrum of the nucleus in a high-flux state, which is different from that in [Gulati et al. \(2023\)](#). The Fermi-LAT spectrum is derived from the analysis conducted in this study, same as in Figure 2(a).